

Structure of the Si{100} surface in the clean (2×1), (2×1)-H monohydride, (1×1)-H dihydride, and c(4×4)-H phases

Y. Wang, M. Shi, and J. W. Rabalais

Department of Chemistry, University of Houston, Houston, Texas 77204-5641

(Received 8 September 1992; revised manuscript received 8 February 1993)

The structure of the Si{100} surface in the clean (2×1), (2×1)-H monohydride, (1×1)-H dihydride, and c(4×4)-H phases has been studied by time-of-flight scattering and recoiling spectrometry. The hydrogenated phases were formed by saturation exposure to atomic hydrogen at room temperature for (1×1), ≈400°C for (2×1), and ≈620°C for c(4×4). Time-of-flight spectra of scattered and recoiled neutrals plus ions were collected as a function of crystal azimuthal angle and primary-beam incident angle to the surface. Structural analyses of the phases were obtained from the azimuthal anisotropy of the recoiled silicon-atom flux from 4 keV Ar⁺ primary ions and from the critical incident angles for 4-keV Ne⁺ primary ions scattering along selected azimuths. Analysis of shadowing and blocking effects in these scattering and recoiling events, using calibrated shadow cones, is used in the structure determinations. The data provide a direct determination of the interatomic spacings in the outermost silicon layer of the four surface phases investigated.

I. INTRODUCTION

The Si{100} surface has been studied extensively over the past two decades using various theoretical¹⁻¹¹ approaches and all of the experimental¹²⁻³² techniques known to surface science (see Ref. 33 for reviews). Despite this enormous effort, structural details at the atomic level remain controversial for both the clean surface and the various hydrogen-induced surface phases. The difficulty arises from the complicated reconstructions involving large displacements of atoms from their bulk positions. This is the first of a pair of papers concerning the structure of Si{100} and hydrogen on its surface. The purpose of this paper is to present the application of the technique of time-of-flight scattering and recoiling spectrometry (TOF-SARS) to determination of the Si surface structure of Si{100} in the clean (2×1), (2×1)-H monohydride, (1×1)-H dihydride, and c(4×4)-H phases. The following paper³⁴ presents the application of TOF-SARS to determination of the hydrogen structure on these various phases of Si{100}.

The clean Si{100} surface undergoes a (2×1) reconstruction. For this (2×1) surface, it is generally accepted that the first-layer Si atoms dimerize along the (01 $\bar{1}$) azimuth, thus doubling the repeat length along this direction. However, there still exists some uncertainty concerning the actual configuration of the surface dimers and their intradimer spacing. The models that have been formulated can be classified into two categories, i.e., buckled asymmetrical and simple symmetrical dimers. The buckled dimer model was favored by early theoretical and experimental studies, while more recent works tend to favor the simple symmetrical dimer model, although both models have been the subject of ongoing discussions in the literature. Scanning tunneling microscopy (STM) studies^{28,29} have found symmetrical dimers on defect-free terraces and buckled dimers or zigzag structures near

monoatomic steps. Recent molecular-dynamics simulations³¹ have provided evidence for subpicosecond interconversion of buckled and symmetric dimers. This finding has been supported by low-temperature STM images.³⁵ These images show that at low temperature the number of buckled dimers increases while at high temperature the dimers rapidly switch orientation, leading to an averaged symmetric appearance in STM images. Concerning the intradimer spacing, typical reported values are 2.3–2.5 Å from experimental measurements^{12,32} and 2.1–2.4 Å from theoretical calculations.^{2-4,7}

Exposure of the Si{100} surface to a saturation dose of H atoms at ≈400°C produces a hydrogenated surface which retains its (2×1) periodicity. It is proposed that H atoms react with the single dangling bond of each Si atom in the dimerized surface to produce a monohydride with a coverage of 1.0 monolayer (ML). The structure of this surface has been shown³⁰ to be well ordered and stable in the presence of atomic H. To the best of our knowledge, the intradimer spacing in this monohydride phase has not been determined experimentally.

Exposure of the Si{100} surface to a saturation dose of H atoms at room temperature produces a (1×1) low-energy electron diffraction (LEED) pattern with a diffuse background. The structure of this surface has been problematic. It was originally believed^{15,16} that the surface was bulklike and a dihydride phase was formed by H atoms bonding to the two dangling bonds of every Si atom. Experimental observation of a saturation coverage less than 2.0 ML raised doubts about this model.²¹ Subsequently, it was suggested²⁴ that the surface consists of a disordered (3×1) phase consisting of alternating monohydride and dihydride units. Recent H exposure studies¹⁸ have found a saturation coverage of 1.85±0.18 ML, supporting a dihydride structure. STM results³⁰ for the H saturated surface indicate a (1×1) dihydride phase which is poorly ordered and susceptible to spontaneous

etching by H atoms. The (3×1) phase is suggested^{27,30} to be a H-induced reconstruction which exists only under special conditions.

The $c(4 \times 4)$ -H phase of Si{100} has received much less attention than the other phases. This surface can be produced in a number of ways,^{36,37} one of which consists of exposure to H atoms while the sample is at $\approx 620^\circ\text{C}$. It is proposed that the high hydrogen exposure produces missing-dimer defects by vaporization of volatile silane and that subsequent annealing orders these missing-dimer defects. LEED analysis^{36,37} suggests an ordered structure of missing-dimer defects formed on the basic (2×1) structure.

In view of the remaining uncertainties concerning the structures of these technologically important surfaces, we have applied the technique of time-of-flight scattering and recoiling spectrometry³⁸ to determine the structure of the outermost atomic layer of silicon in these four different phases. We assume as a starting point, based on LEED and STM results, that both the clean (2×1) and (2×1) -H surfaces are dimerized along the $\langle 01\bar{1} \rangle$ azimuth.

This study of the silicon surface uses the method of Si atom recoil detection. Since the atoms are ejected from the surface sites that they occupy in the lattice, the trajectories are simple and direct structural information is obtained. This recoiling method is extremely sensitive to the outermost atomic layer of a surface and, therefore, is ideal for determining the configuration of the dimers and the H-induced structures. Coupling this recoiling method with ion scattering from the surface makes it possible to determine the periodicities of the various surface phases, the intradimer atomic distances, and the dimer configuration.

II. EXPERIMENT

A. Description of the TOF-SARS technique

Time-of-flight scattering and recoiling spectrometry (TOF-SARS) has been detailed in a previous publication.³⁹ In short, it consists of bombarding a sample with keV rare-gas ions and detecting the scattered and recoiled neutrals plus ions. Anisotropies in the scattered and recoiled particle fluxes as a function of the crystal azimuthal and beam incidence angles are interpreted in terms of shadowing, blocking, and focusing effects. These effects arise from the fact that in the keV energy range, interatomic interactions between projectiles and target atoms are governed by repulsive potentials. As a result, regions which projectiles cannot penetrate are created behind the target atoms, effectively masking other target atoms that would be located inside such a region from the incident beam. These regions are referred to as shadowing or blocking cones, depending on whether they act on the incoming or outgoing particle trajectories, respectively. An important property of these cones is that focusing of the particle trajectories occurs at the edge of the cones, giving rise to further anisotropies in the flux distributions.

The instrumental details employed are as follows. Pri-

mary 4-keV Ne^+ and Ar^+ beams are pulsed onto the sample in a UHV chamber at a 30-kHz rate, with a 30-ns pulse width, and an average current density of 0.1 nA/mm². The scattered and recoiled particles are velocity analyzed through a 120-cm-long time-of-flight drift tube and both the neutral and charged particles are detected with a channel electron multiplier. The signal is amplified, discriminated, and fed to the stop input of a time-to-amplitude converter (the start input being provided by the pulse generator). The signal is then analyzed with a multichannel pulse height analyzer and displayed as particle distribution versus time of flight. The scattered and recoiled intensities are obtained by integrating narrow time windows under the corresponding TOF peaks. All TOF spectra were acquired with the sample at room temperature.

Collection of both ions and neutrals in the TOF mode provides two important advantages. First, the technique is relatively nondestructive due to the efficient collection of both ions and neutrals in the TOF mode. Spectra can be acquired with an ion dose of $< 10^{-3}$ primary ions/surface atom. Second, the problem of unknown ion-surface neutralization probabilities is eliminated. It has recently been shown⁴⁰ that the survival probabilities of scattered noble gas ions have a strong azimuthal dependence.

B. Sample preparation

Several different samples were used. Each one consisted of a 10×15 mm Si{100} wafer which was cleaned according to the procedure described by Ishizaka and Shiraki.⁴¹ Extended heating in UHV at $> 1000^\circ\text{C}$ produced a sharp (2×1) LEED pattern with no impurities detectable by TOF-SARS. Hydrogen adsorption on this surface was achieved by exposure to H atoms produced by dissociation of molecular H_2 on a tungsten filament at $\approx 1500^\circ\text{C}$ positioned ≈ 10 cm in front of the sample. TOF-SARS spectra of these surfaces revealed H recoils but no impurity C and O recoils.

The (2×1) -H monohydride and (1×1) -H dihydride surfaces were produced by saturation exposure of the clean surface to 1.0×10^{-6} torr H_2 at $\approx 400^\circ\text{C}$ and room temperature, respectively. The (2×1) -H monohydride surface produced a sharp LEED pattern repeatedly. For the (1×1) -H dihydride surface, sharp LEED patterns were produced only intermittently, depending on the subtleties of the heating and exposure procedure; measurements were made only on surfaces with sharp LEED patterns. The $c(4 \times 4)$ -H surface was obtained by three different methods: (i) exposing to 1×10^{-6} torr H_2 with the sample at $\approx 620^\circ\text{C}$, (ii) formation of the (1×1) -H surface and then annealing at $\approx 620^\circ\text{C}$, and (iii) taking a surface that was recently exposed to H atoms, heating it to $> 1000^\circ\text{C}$, and annealing it at $\approx 620^\circ\text{C}$ in the absence of hydrogen. Method (i) gave the sharpest $c(4 \times 4)$ LEED pattern. Method (iii) produced the $c(4 \times 4)$ pattern for only the first few heating cycles, after which it was necessary to redose with H atoms in order to achieve the pattern. This suggests that there may be subsurface hydrogen. The $c(4 \times 4)$ structure could be converted into the

(1×1) dihydride structure by saturation exposure of atomic hydrogen at room temperature. Examples of the LEED patterns obtained are shown in Fig. 1.

III. EXPERIMENTAL RESULTS

A. Time-of-flight spectra

Examples of typical TOF spectra obtained from 4-keV Ar^+ impinging on a $\text{Si}\{100\}$ -(2×1) surface are shown in Fig. 2. Peaks due to scattered argon and recoiled hydrogen, carbon, oxygen, and silicon are observed on the uncleaned surface. These TOF peaks are identified by application⁴² of the classical binary elastic collision model. Only the scattered Ar and recoiled Si peaks are observed

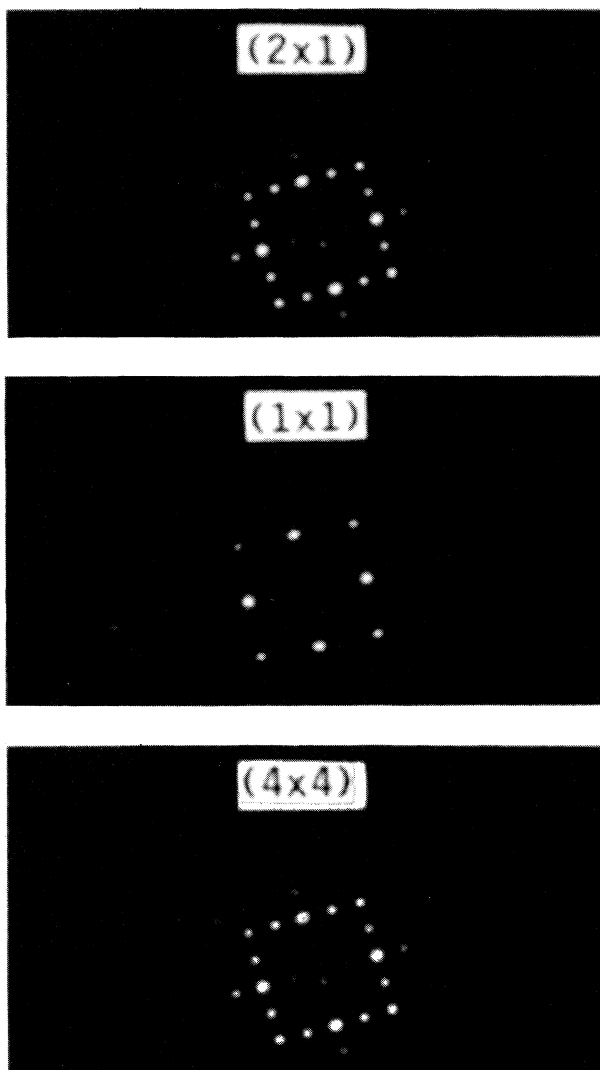


FIG. 1. Observed LEED patterns for the (2×1)-H, (1×1)-H, and *c*(4×4)-H phases of $\text{Si}\{100\}$. The (2×1) pattern represents a superposition of two structural domains, i.e., (2×1) and (1×2), rotated by 90°. The LEED pattern of the clean (2×1) surface is similar to that shown here for the (2×1)-H surface. Electron energy is 50 eV.

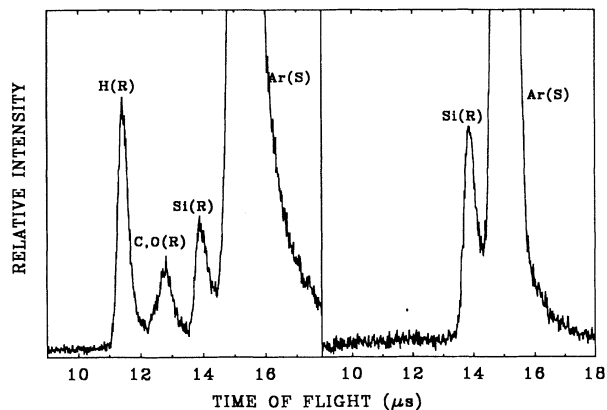


FIG. 2. Time-of-flight spectra of an unclean (left) and clean (right) $\text{Si}\{100\}$ surface showing the scattered Ar and recoiled H, C, O, and Si features. Conditions: 4-keV Ar^+ , $\Theta=28^\circ$, $\alpha=8^\circ$, and $\delta=15^\circ$.

after cleaning the surface in UHV. Scattered Ar corresponds to quasisingle scattering of Ar from Si, i.e., the projectile experiences one large-angle deflection (small impact-parameter p collision), which may be preceded or followed by minor deflections. Recoiled atoms are those that are directly recoiled from a quasisingle collision of an impinging Ar^+ , i.e., small-angle deflections may precede and follow the close collision. The positions of these peaks are not sensitive to the incident α and azimuthal δ orientations of the sample and very close to the TOF predicted by the binary collision model, indicating that the major contributions to these peaks are from single collision events. The broadening of the scattered Ar peak on the long TOF side is due to multiple scattering. The recoiled silicon intensity $\text{Si}(R)$ was obtained by integrating the area under the Si recoil peak following background subtraction.

B. Clean $\text{Si}\{100\}$ -(2×1) surface

1. Azimuthal angle δ scans of $\text{Si}(R)$ in the shadowing mode

The azimuthal patterns of the recoiled Si atoms were obtained in the shadowing mode,^{43,44} i.e., the primary Ar^+ beam was directed at a glancing incident angle α and, as the crystal is rotated azimuthally, the recoiled Si flux $\text{Si}(R)$ is monitored in off-specular conditions where the scattering and recoiling angles (Θ and ϕ) are considerably higher than 2α . Using the recoil angle of $\phi=28^\circ$, the recoil trajectory is above the blocking cones for recoil of first-layer atoms and the azimuthal dependence is controlled by shadowing of the incident ions. For azimuths along which the first-layer atoms are directly aligned, the shadow cones of the closely spaced atoms prevent the ion trajectories from penetrating below the first-atomic layer. Therefore, the impact parameters (p) that are necessary for recoiling of first-layer atoms out of the surface are unattainable. As a result, minima in $\text{Si}(R)$ are observed along the directions for which the first-layer atoms are

aligned. Along intermediate axes where the interatomic spacings are longer, such p values are accessible and maxima in $\text{Si}(R)$ are observed.

An azimuthal scan of the Si recoils is shown in Fig. 3. The $\text{Si}(R)$ variation with δ reveals the surface periodicity. The pattern is symmetrical about the $\langle 011 \rangle$ or $\langle 01\bar{1} \rangle$ ($\delta=0^\circ$) azimuth. The positions of the minima (A), (B), and (D) correspond to alignment of first-layer atoms while the minima (C) have both first- and second-layer contributions. The positions of these minima and the repetition of the symmetry features every 90° are consistent with a surface that has two domains which are rotated 90° with respect to each other. The alignments of the atoms in the two domains that contribute to these minima are indicated in the structural drawings.

The widths of the minima are related to the interatomic spacings along that particular direction. The smaller the interatomic spacing, the wider the minimum because of the larger degree of rotation about δ required for atoms to emerge from the shadow of their preceding neighbor. The wide minimum (A) is a direct result of the short interatomic spacing between the dimers along the $\langle 01\bar{1} \rangle$ azimuth. The shallow, narrow minima (C) result from the long interatomic first- and second-layer spacings along the $\langle 001 \rangle$ and $\langle 010 \rangle$ azimuths.

The minima (B and D) were used to obtain the registry

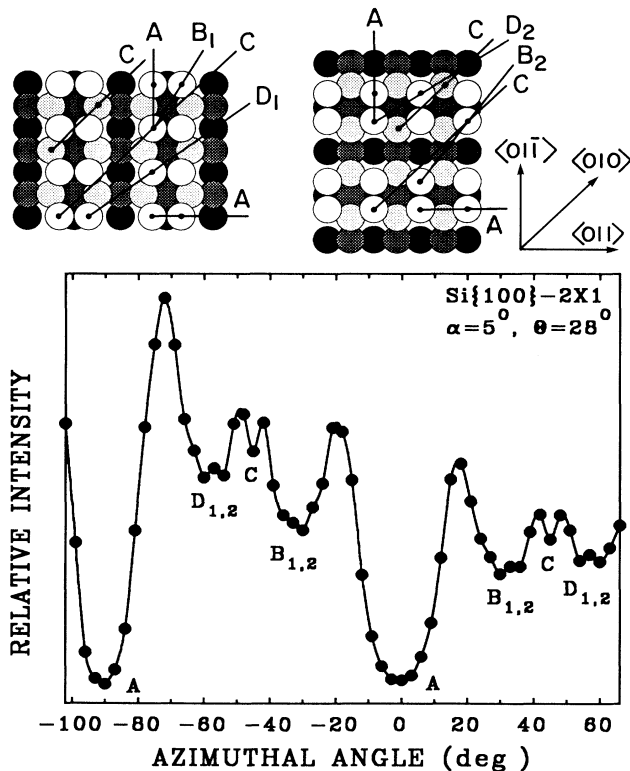


FIG. 3. Azimuthal angle δ scan of silicon recoil intensity $\text{Si}(R)$ for the clean (2×1) surface. The minima are identified from the two domains (rotated by 90°) of the structural drawings.

of the dimers with respect to the underlying lattice. Measuring these regions, which are symmetrically dispersed about $\delta=0^\circ$, in increments of $\Delta\delta=1^\circ$ indicates that each region actually contains three minima, labeled B_1 , B_2 , and B_3 and D_1 , D_2 , and D_3 as shown in Fig. 4. Deconvolutions of the overlapping peaks using Gaussian peak shapes are shown in the lower part of the figure. For comparison with the structural drawings, it is observed that the B_1 , B_2 , D_1 , and D_2 minima correspond to the alignment of atoms in neighboring Si dimers in the two domains. The minor B_3 and D_3 minima correspond to alignment of second-nearest-neighbor Si atoms in the dimers. Note that the widths of the B_1 and D_1 deconvoluted minima are larger than those of the B_2 and D_2 minima, in accord with the inverse relationship between the widths and the interatomic spacings as discussed above. The positions of these $B_{1,2}$ and $D_{1,2}$ minima are listed in Table I. Since the first-layer atoms dimerize along $\langle 01\bar{1} \rangle$, the interatomic distance along $\langle 011 \rangle$ remains bulklike, i.e., 3.84 \AA . Using simple geometry, the intradimer bond lengths are determined as listed in Table I. Averaging these values provides an intradimer spacing of $2.26 \pm 0.10 \text{ \AA}$. This intradimer bond length was used to calculate all of the azimuthal orientations for alignment of first-layer Si atoms; the results are compared to the positions of the experimental minima in Table II. There is excellent agreement between the calculated and experimental minima.

2. Incident angle α scans of $\text{Ne}(S)$

Monitoring the Ne scattering intensity $\text{Ne}(S)$ as a function of α along selected azimuths provides information⁴³ on the interatomic spacings d along those crystallographic directions. At grazing α , all atoms lie within the

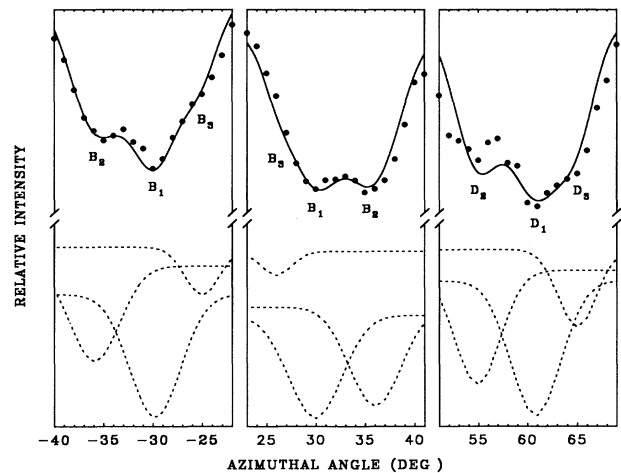


FIG. 4. Details of the azimuthal angle δ scan of silicon recoil intensity $\text{Si}(R)$ for the minima labeled $B_{1,2}$ and $D_{1,2}$ in Fig. 3. The dashed curves are deconvoluted peaks and the solid line through the data points is the sum of the deconvoluted curves.

TABLE I. Calculation of intradimer spacings from the deconvoluted azimuthal minima of the δ scans.

Minimum	Minimum δ value (deg)	Calculated Intradimer spacing (\AA)
Si{100}-(2 \times 1) surface; minima (B_1 and B_2 and D_1 and D_2) of Figs. 3 and 4		
B_1	-29.8 ± 1.0	2.20 ± 0.10
	29.9 ± 1.0	2.21 ± 0.10
B_2	-35.9 ± 1.0	2.37 ± 0.10
	36.0 ± 1.0	2.40 ± 0.10
D_1	60.8 ± 1.0	2.15 ± 0.10
D_2	54.9 ± 1.0	2.22 ± 0.10
		Average 2.26 ± 0.10
Si{100}-(2 \times 1)-H monohydride surface; minima (C_1) from Figs. 8 and 9		
C_1	38.0 ± 1.0	3.00 ± 0.10
	37.3 ± 1.0	2.93 ± 0.10
		Average 2.97 ± 0.10

shadow cones of their preceding neighbors precluding small p collisions; as a result, no large angle scattering can occur and $\text{Ne}(S)$ is negligible. As α is increased, first-layer atoms move out of the shadow cones of their first-layer neighbors. When the p value required for scattering into Θ becomes accessible, a sharp increase in $\text{Ne}(S)$ is observed. This sharp increase in $\text{Ne}(S)$ results from a combination of two factors, i.e., accessibility of previously shadowed scattering centers to the ion beam and focusing of incoming Ne trajectories at the edges of the shadow cones. Subsequent increases in α result in decreases in $\text{Ne}(S)$ due to loss of the focusing effect.

The critical incident angles α_c , defined as the α value at half peak height, can be related⁴² to the interatomic distance d through the use of calibrated shadow cones. For a given scattering process, α_c is related to d and the inclination angle α_i of the bond direction to the surface according to

$$L = d \times \cos(\alpha_c + \alpha_i) \quad (1)$$

and

$$R = d \times \sin(\alpha_c + \alpha_i) + p. \quad (2)$$

Here L is the distance behind the shadowing center, R is the shadow cone radius, and p is the impact parameter necessary to scatter Ne into Θ . The 4-keV $\text{Ne} \rightarrow \text{Si}$ shadow cone was calculated from the Moliere potential and Firsov's screening length.⁴⁵ The screening constant C was varied to obtain agreement with the experimentally determined α_c for a known d value. This was accomplished by measuring α_c for the Si{100}-(1 \times 1)-H surface along the principal azimuths at $\delta = 0^\circ$ ($\langle 011 \rangle$ and $\langle 01\bar{1} \rangle$) from the mixed domains and $\delta = 45^\circ$ ($\langle 010 \rangle$) as shown in Fig. 5 and adjusting C to fit the bulk Si-Si spacing. The (1 \times 1)-H surface phase was used for this calibration because all of the first-layer Si-Si spacings along a given azimuth are identical for this surface. The presence of H is

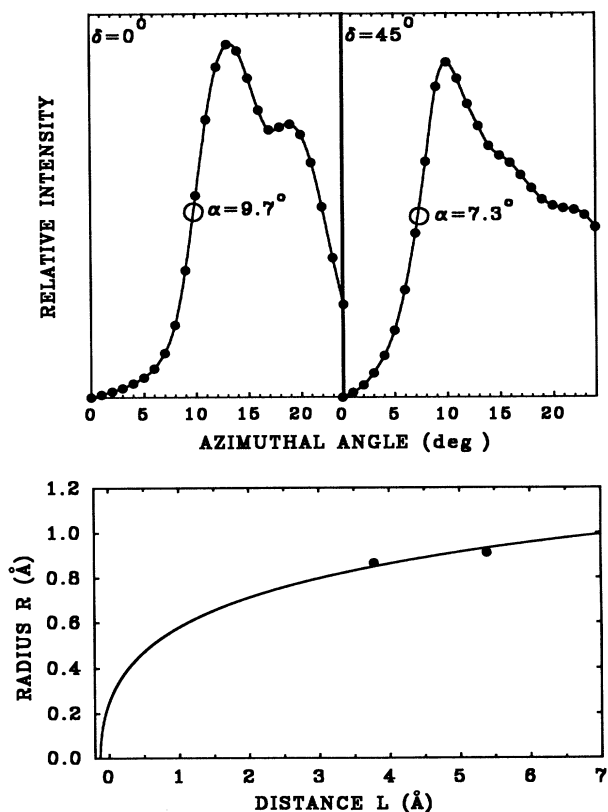


FIG. 5. (Top) Incident angle α scans of 4-keV Ne scattering intensity $\text{Ne}(S)$ at $\Theta = 34^\circ$ along the $\delta = 0^\circ$ ($\langle 011 \rangle$ and $\langle 01\bar{1} \rangle$) and $\delta = 45^\circ$ ($\langle 010 \rangle$) azimuths for the Si{100}-(1 \times 1)-H surface showing the critical incident angles α_c used for calibration of the shadow cone. (Bottom) Calibrated shadow cone plotted as the radius of the cone R vs distance behind the target atom L . The two experimental points from the α scans used for calibration are indicated.

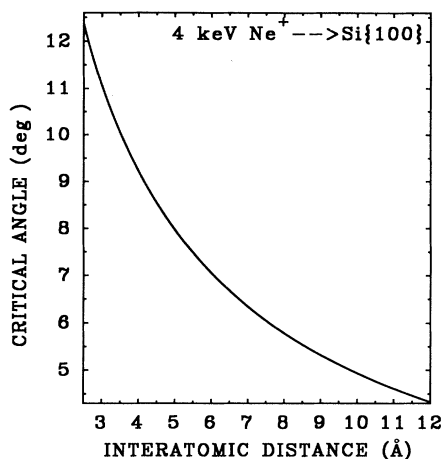


FIG. 6. Plot of the calculated critical incident angle α_c for 4-keV Ne scattering from Si vs the Si-Si interatomic spacing.

a negligible perturbation on the Ne trajectories at the scattering angle $\Theta = 34^\circ$ used. The value of the screening constant which gave the best fit (see Fig. 5) to the experimental data was $C = 0.68$. The resulting calculated curve for α_c versus interatomic distance d is shown in Fig. 6.

An α scan was carried out along $\delta = 30^\circ$ (the B_1 direction of Fig. 3), i.e., the alignment direction for near-side and far-side dimer atoms, as shown in Fig. 7. The critical angle from Fig. 7 is $\alpha_c(\text{exp}) = 7.5^\circ$. From the intradimer distance of 2.26 \AA determined above, the Si-Si distance along $\delta = 30^\circ$ is 4.46 \AA for a symmetrical dimer; using the calibrated shadow cone, this spacing corresponds to a critical angle of $\alpha_c(\text{calc}) = 8.2^\circ$. The $\alpha_c(\text{exp})$ is less than the $\alpha_c(\text{calc})$ because there are some long interatomic spacings near $\delta = 30^\circ$ which contribute to Ne(S). If the dimer would be buckled by a vertical shift of one of the atoms upward by 0.1, 0.2, or 0.3 Å , the $\alpha_c(\text{calc})$ value

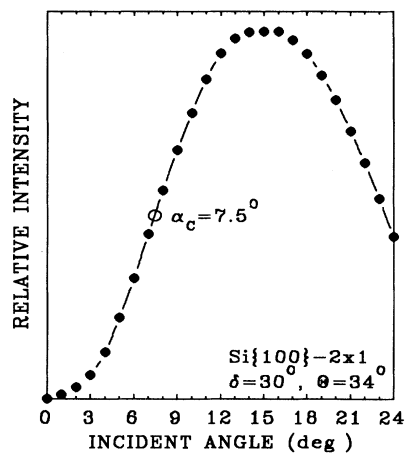


FIG. 7. Incident angle α scan along $\delta = 30^\circ$ [B_1 minimum for the clean (2×1) surface] showing the critical incident angle α_c determined between near- and far-side dimers as shown in the structural diagram of Fig. 3.

would shift down to 7.1° , 5.8° , or 4.5° , respectively; the latter two values are well outside of the experimental uncertainty and the former value is at the uncertainty limit. These data are therefore consistent with a symmetrical dimer arrangement, however a vertical buckling $< 0.1 \text{ \AA}$ cannot be ruled out.

C. Si{100}-(2×1)-H monohydride surface

The azimuthal pattern of Si recoils from the $\approx 400^\circ$ hydrogen saturated surface is shown in Fig. 8. The perturbation of the Ar and Si trajectories by H atoms can be neglected because the maximum deflections are only $\sim 1.4^\circ$ and $\sim 2.1^\circ$, respectively. The observed periodicity indicates that the outermost layer of Si atoms are in a (2×1) dimerized array as shown from comparison with the structural diagrams of Fig. 8. However, compared to the clean surface (2×1) pattern of Fig. 3, there are distinct differences. The positions of the minima, as listed in Table I, are significantly different in both cases. The azimuthal pattern of Fig. 8 is consistent with a (2×1) structure in which the intradimer bond length is larger than that of the clean surface. The minima in Fig. 8 define the registry of the dimers with respect to the underlying lattice. Measuring these regions in increments of $\Delta\delta = 1^\circ$, as shown in Fig. 9, indicates that there are two

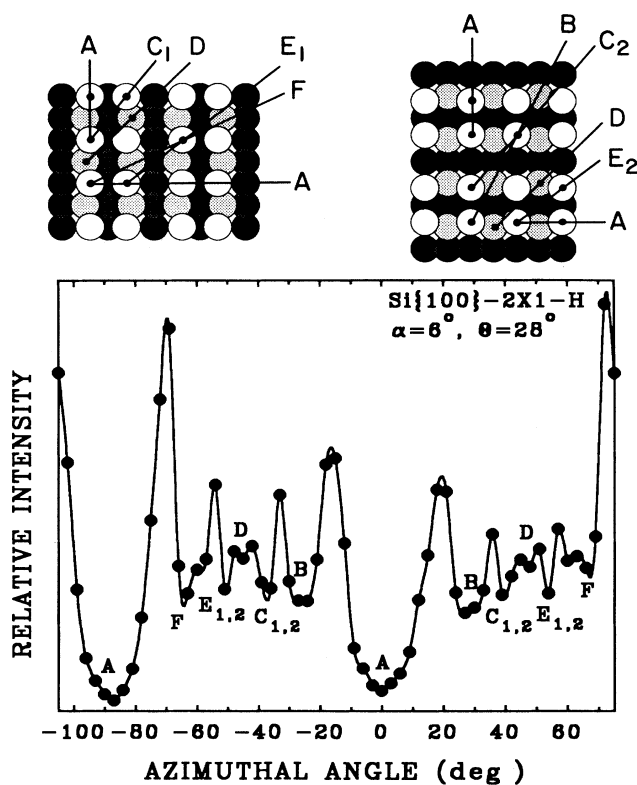


FIG. 8. Azimuthal angle δ scan of silicon recoil intensity Si(R) for the (2×1) -H monohydride surface. The minima are identified from the two domains of the structural drawing. The hydrogen atoms are not shown.

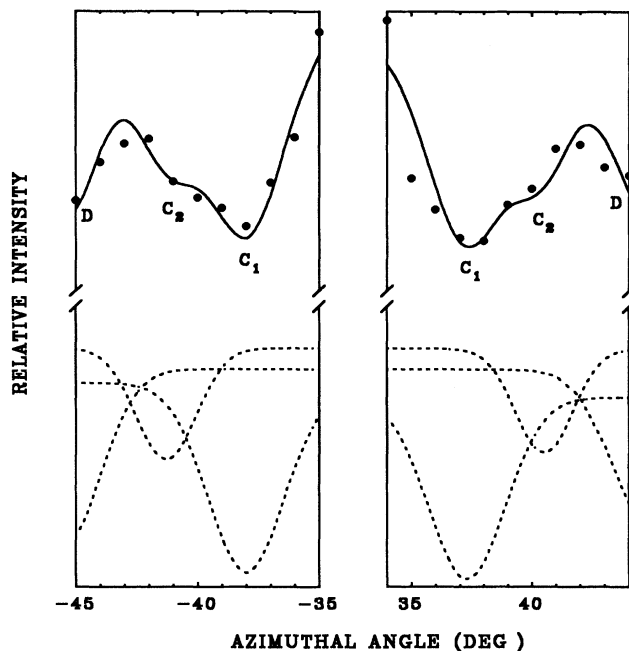


FIG. 9. Details of the azimuthal angle δ scan of silicon recoil intensity $\text{Si}(R)$ for the minima labeled $C_{1,2}$ in Fig. 8 for the (2×1) -H surface. The dashed curves are deconvoluted peaks and the solid line through the data points is the sum of the deconvoluted curves.

pairs of minima ($C_{1,2}$). Deconvolutions of the overlapping peaks using Gaussian peak shapes are shown in the lower part of the figure. Note that the widths of the C_1 and C_2 minima are inversely proportional to the interatomic spacings. From comparison with the structural drawings, these two pairs of minima correspond to the alignment of atoms in neighboring Si dimers in the two domains. Since the first-layer atoms dimerize along $\langle 01\bar{1} \rangle$, the interatomic distance along $\langle 011 \rangle$ remains bulklike, i.e., 3.84 Å. Using only the sharp minima (C_1) and simple geometry, the intradimer bond lengths are determined as 2.97 ± 0.10 Å. The positions of the other minima were calculated from this intradimer bond length; the results are compared to the positions of the experimental minima in Table II. There is excellent agreement between the calculated and experimental minima.

D. $\text{Si}\{100\}$ -(1×1)-H dihydride surface

The azimuthal pattern of Si recoils from the room-temperature hydrogen-saturated surface is shown in Fig. 10. The observed periodicity indicates that the outermost layer of Si atoms is in a (1×1) bulklike array as shown from comparison with the structural diagrams of Fig. 10. Compared to the δ scans of the clean and monohydride (2×1) surfaces in Figs. 3, 8, and 9, there are several distinct differences. (i) The positions of the minima [$(B_{1,2})$ and $(D_{1,2})$ for the clean (2×1) and $(C_{1,2})$ and $(E_{1,2})$ for the (2×1) -H surfaces] are shifted from pairs of minima

to single minima at $\pm 24^\circ$ and $\pm 63^\circ$, respectively, on the (1×1) surface. (ii) The large minimum (A) at $\delta = 0^\circ$ is narrower in the very bottom of the minimum for the (1×1) surface because the removal of the Si dimers restores the interatomic spacings to the longer bulklike distance. (iii) The minima (C) along the $\langle 010 \rangle$ and $\langle 001 \rangle$ azimuths ($\delta = \pm 45^\circ$) are much deeper and wider than those of the (2×1) surfaces. This is because all of the first- and second-layer Si atoms are aligned in this direction on the (1×1) surface.

The azimuthal pattern is also compared with a previously proposed²⁴ (3×1) surface structure consisting of alternating monohydride and dihydride units in Fig. 10. Table II compares the experimental minima with the positions of minima calculated from the (1×1) and (3×1) models. The (1×1) structure is in excellent agreement with the experimental data. The (3×1) structure is not in good agreement with the observed azimuthal anisotropy because the predicted pattern of the δ minima is different from that observed experimentally.

E. $\text{Si}\{100\}$ - $c(4 \times 4)$ -H surface

The azimuthal pattern of the Si recoils from the $c(4 \times 4)$ -H surface is shown in Fig. 11. The observed periodicity is different from that of the other surfaces and certainly more complicated than that of a (1×1) structure. Four different missing-dimer models considered as possible structures giving rise to the observed $c(4 \times 4)$ pattern were used as models. These models, shown in Fig. 12, are (a) crosswise linked dimers (CLD), (b) one missing dimer (1MD), (c) two missing dimers (2MD), and (d) three missing dimers (3MD). The calculated and experimental minima positions are listed in Table II. The calculated positions were optimized for best agreement with the experimental positions by varying the intradimer bond lengths. From Table II, the 2MD and 3MD models can be ruled out because they do not give the major minima observed at positions (B) and (F) in Fig. 11. The 1MD and CLD models provide equally good fits to the observed positions of the azimuthal minima. Considerations of the depths of the minima favor the CLD model as follows. (i) The (C) minima should be deep for 1MD [comparable to the (B) minima of Fig. 3] due to the short interatomic spacings and shallow for CLD due to the long spacings; this favors the CLD model. (ii) The (B) minima should be shallow for 1MD because of the single long spacing and deep for CLD due to the short and long spacings; this favors the CLD model. Also, the (B) minima are observable even as high as $\alpha = 7^\circ$, which is only possible for interatomic spacings $\lesssim 4.5$ Å; the first-layer Si spacings along the (B) directions are ≈ 4.1 Å for CLD and ≈ 8.1 Å for 1MD. (iii) The deep (D) minima are consistent with alignment of closely spaced first- and second-layer atoms along $\delta = 45^\circ$, which also favors CLD over 1MD. Using the CLD model, an intradimer distance of 2.5 ± 0.2 Å (Table II) provides best agreement with the experimental data.

The incident angle α scans of the scattered Ne intensity $\text{Ne}(S)$ also favor the CLD model. An α scan along $\delta = 19^\circ$ corresponding to the $B_{1,2}$ alignment of Fig. 11 is

TABLE II. Measured and calculated minima for the silicon recoil azimuthal angle δ scans of the four surface phases of Si{100} investigated. The models are determined by varying the first-layer interatomic spacings to obtain the best agreement between experimental and calculated minima. The structure and bond lengths which provided the calculated positions listed here are those indicated in the text.

Minimum		Clean Si{100}-(2×1)								
		A	B ₁	B ₂	C	D ₁	D ₂			
Expt.	0.0°±3.0°	29.9°±1.0°	35.9°±1.0°	45.0°±3.0°	54.9°±1.0°	60.8°±1.0°				
Calc.	0.0°	29.6°	34.9°	45.0°	55.1°	60.4°				
Minimum		Si{100}-(2×1)-H monohydride								
		A	B	C ₁	C ₂	D	E ₁	E ₂	F	
Expt.	0.0°±3.0°	25.5°±3.0°	37.7°±1.0°	40.0°±1.0°	45.0°±3.0°	52.5°±3.0°	52.5°±3.0°	64.5°±3.0°	87.0±3.0°	
Calc.	0.0°	26.6°	38.0°	39.4°	45.0°	50.6°	52.0°	63.4°	90.0°	
Minimum		Si{100}-(1×1)-H dihydride								
		A	B	C						D
Expt.	0.0°±1.0°	24.0±3.0°	45.0°±3.0°						63.0±3.0°	
Calc. (1×1)	0.0°	26.6°	45.0°						63.4°	
Calc. (3×1)	0.0°	26.0°	30.0°	31.1°	35.5°	45.0°	54.9°	60.0°	63.4°	
Minimum		Si{100}-c(4×4)-H								
		A	B ₁	B ₂	C	D	E	F	A-90°	
Expt.	0.0°±3.0°	19.5°±3.0°	34.0°±1.0°	46.5°±3.0°	57.0°±3.0°	70.5°±3.0°	88.5°±3.0°			
CLD ^a	0.0°	18.0°	19.2°	34.0°	45.0°	56.0°	70.8°	72.0°	90.0°	
1MD ^a	0.0°	18.6°	33.5°	34.0°	37.0°	53.0°	56.0°	71.4°	90.0°	
2MD ^a	0.0°		33.5°	34.0°	45.0°	56.0°	56.5°	90.0°	90.0°	
3MD ^a	0.0°		33.5°	36.7°	45.0°	53.2°	56.5°	90.0°	90.0°	

^aCLD, crosswise linked dimers; 1MD, one missing-dimer model; 2MD, two missing-dimer model; 3MD, three missing-dimer model.

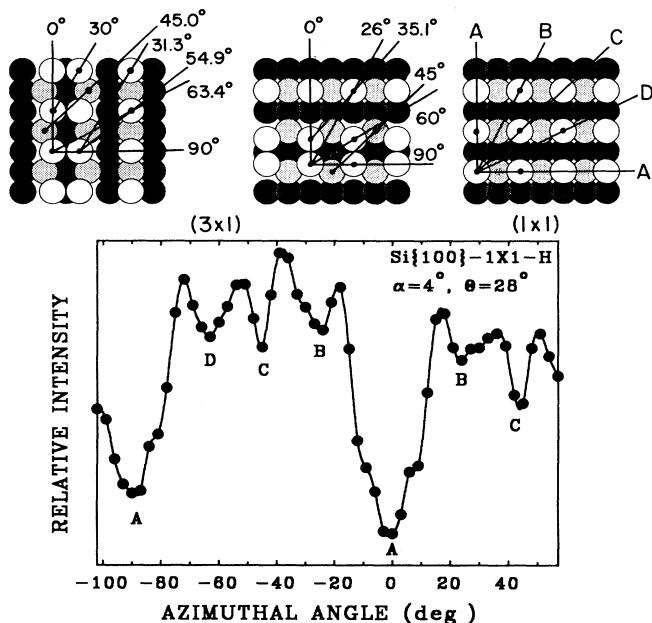


FIG. 10. Azimuthal angle δ scan for the (1×1) -H dihydride surface. The minima are identified according to the (1×1) structural model. A (3×1) structural model consisting of alternating monohydride and dihydride units is also shown. The hydrogen atoms are not shown.

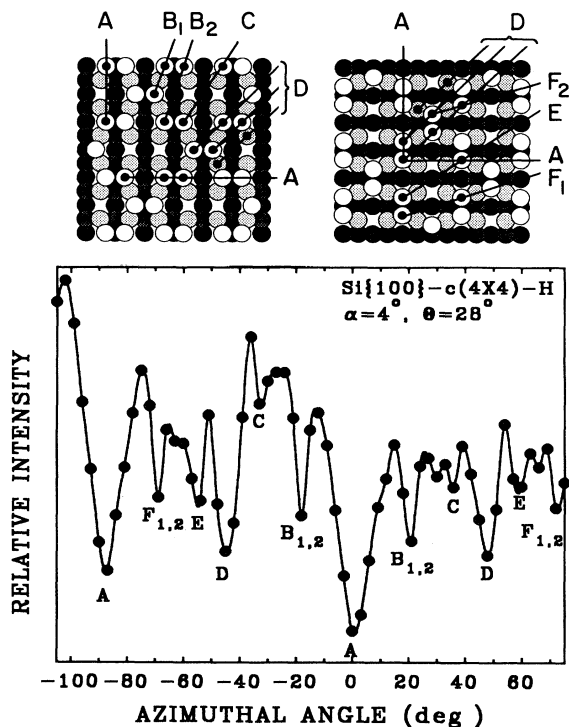


FIG. 11. Azimuthal angle δ scan of silicon recoil intensity $\text{Si}(R)$ for the $c(4 \times 4)$ -H surface. The minima are identified from the two domains of the structural drawing. The hydrogen atoms are not shown.

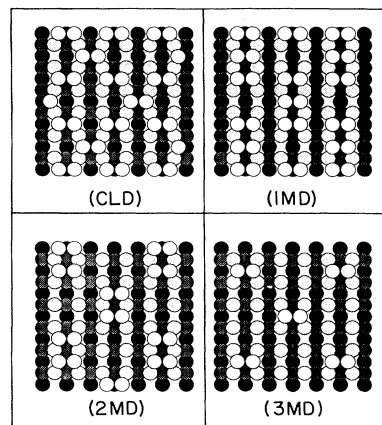


FIG. 12. Four structural models considered for the $c(4 \times 4)$ structure. CLD, crosswise linked dimers; 1MD, one missing dimer; 2MD, two missing dimers; 3MD, three missing dimers.

shown in Fig. 13. The $\alpha_c = 8.7^\circ$ value corresponds to an interatomic spacing of 4.1 \AA (Fig. 6) along $\delta = 19^\circ$ and a corresponding intradimer spacing of 2.3 \AA , in qualitative agreement with the value determined from the δ scan above. The intradimer spacing determined from the δ scan (Fig. 11) is the most accurate since the α scan (Fig. 14) has contributions from different Si-Si distances. For the 1MD model, the interatomic distance along $\delta = 18.6^\circ$ is $\approx 8.1 \text{ \AA}$, corresponding to $\alpha_c = 5.7^\circ$ (Fig. 6); this is far outside of the experimental uncertainty of Fig. 13.

IV. DISCUSSION

Detection of recoiled Si atoms by the TOF-SARS technique is capable of providing unambiguous determinations of the structures of various $\text{Si}\{100\}$ surface phases. This was discovered only after attempting several other

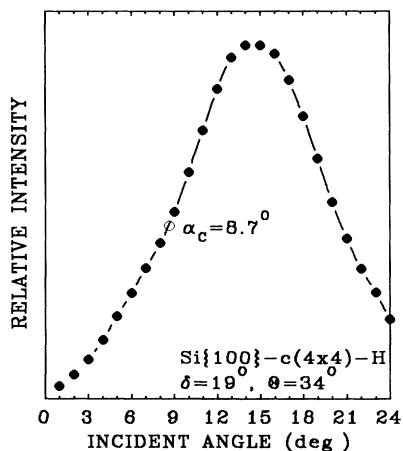


FIG. 13. Incident angle α scan of the scattered Ne intensity $\text{Ne}(S)$ along $\delta = 19^\circ$ (minima B of Fig. 12) for the $c(4 \times 4)$ surface showing the critical incident angle α_c determined between near- and far-side dimers.

methods. *First*, scattering of 1–4-keV He⁺ was attempted. This was unsuccessful because the open structure of the Si{100} lattice resulted in He scattering from several atomic layers. Hence, the surface dimers were only a small fraction of the total scattering centers and the results reflected primarily the bulk interatomic spacings. It has recently been shown that keV He⁺ is scattered from several subsurface atomic layers.⁴⁶ He⁺ scattering may be a good technique to investigate subsurface interfaces or subplanted⁴⁷ atoms. *Second*, Ne⁺ scattering can be done only at small forward angles because Ne loses a large fraction of its energy in collisions with Si, providing poor detection efficiency for neutrals at $\Theta \gtrsim 50^\circ$. The use of such small scattering angles (large impact parameters) and small incident angles (to emphasize first-layer scattering) results in significant Ne multiple-scattering contributions which broaden the azimuthal structural patterns. However, Ne⁺ scattering intensity versus incident angle α scans along selected azimuths were useful in determining interatomic spacings. *Third*, incident angle α scans of Si recoil intensity $S_i(R)$ could not be used for structure determinations for the following reason. For scattering and recoiling angles Θ and $\phi > 40^\circ$, the Si recoiling and Ar scattering peaks overlap, forcing the use of small Θ or ϕ . For Θ or $\phi < 40^\circ$, the α scans for $\alpha > 15^\circ$ are distorted due to blocking along the small exit angle of the recoiling trajectory. As a result of these studies, it was found that δ scans of Si recoiling from Ar⁺ provided the highest sensitivity to the dimer structures in the first layer. Ar⁺ is the choice projectile for recoiling Si rather than Ne⁺ because Ar has a larger shadow cone and a larger recoil cross section for Si atoms.

Our data are consistent with symmetrical dimer structures with intradimer spacings of 2.26 ± 0.10 , 2.97 ± 0.10 , and 2.5 ± 0.2 Å for the clean (2×1), (2×1)-H, and *c*(4×4)-H surfaces, respectively, and a bulklike structure for the (1×1)-H surface. For the clean (2×1) surface, determinations of the intradimer spacings by other experimental techniques^{12,32} are typically in the range 2.3–2.5 Å, whereas theoretical calculations predict spacings in the range 2.1–2.4 Å.^{2–4,7} Our result is therefore in best agreement with some of the theoretical predictions. To the best of our knowledge, there are no experimental determinations of the (2×1)-H intradimer spacing. The finding that the intradimer spacing is larger in the monohydride than in the clean surface is expected, in view of the fact that the H atoms satisfy one of the Si dangling bonds and, as a result, the Si atoms of the monohydride surface are closer to a complete valence shell than those on the clean surface. A bulklike structure is expected for the (1×1)-H surface where both dangling bonds of the terminal Si atoms are hydrogenated. The crosslinked dimer structure found for the *c*(4×4)-H surface is consistent with hydrogen etching of the surface Si atoms, which reduces the surface Si dimer concentration.

In view of the molecular-dynamics calculations of Weakliem, Smith, and Carter,³¹ which show that both symmetrical and asymmetrical dimers coexist and interconvert on a subpicosecond (10–100 fs) time scale, and the STM images of Wolkow,³⁵ which show that at room temperature there is a rapid switching of asymmetric dimer orientations leading to an averaged symmetric appearance, the TOF-SARS observation of symmetrical dimers may be a time-averaged representation of the real surface. Consider the time scale of the TOF-SARS measurements. Primary Ne⁺ and Ar⁺ ions at 4 keV travel 2 Å in about 1 fs. Therefore, individual scattering and recoiling events take place on a shorter time scale than the proposed dimer interconversion time. However a TOF-SARS spectrum is a collection of many of these individual trajectories, which provides a time-averaged representation of the dimer atom positions. This time-averaged representation is consistent with both atoms of the dimer being at the same height above the surface, i.e., symmetrical dimers.

V. CONCLUSIONS

The TOF-SARS technique has been used to characterize the outermost monolayer structures of four surface phases of Si{100}. The lateral structures, i.e., the geometrical models and intradimer spacings, were determined from the positions of the shadowing minima in azimuthal angle scans; these determinations are independent of the model and shadow cone sizes. The symmetrical or buckled nature of the dimers was determined from critical angles in incident angle scans; these determinations are dependent on the shape of the shadow cones, which was calibrated for this specific case. The results are consistent with the following structures.

- (i) The clean Si{100}-(2×1) surface has a symmetrical dimer structure, no detectable buckling, and an intradimer spacing of 2.26 ± 0.10 Å. A buckling amplitude up to 0.1 Å cannot be ruled out.
- (ii) The Si{100}-(2×1)-H monohydride surface has a symmetrical dimer structure, no detectable buckling, and an intradimer spacing of 2.97 ± 0.10 Å. A buckling amplitude up to 0.1 Å cannot be ruled out.
- (iii) The Si{100}-(1×1)-H dihydride surface is terminated in a (1×1) bulklike array in which the interatomic spacings are similar to those of the bulk.
- (iv) The Si{100}-*c*(4×4)-H surface has a crosswise linked dimer structure and intradimer spacings of 2.5 ± 0.2 Å.

ACKNOWLEDGMENTS

This material is based on work supported by the National Science Foundation under Grant No. CHE-881437 and the State of Texas Advanced Research Program under Grant No. 3652022ARP.

- ¹E. Artacho and F. Yndurain, *Phys. Rev. Lett.* **62**, 2491 (1989).
- ²I. P. Batra, *Phys. Rev. B* **41**, 5048 (1990).
- ³M. T. Yin and M. L. Cohen, *Phys. Rev. B* **24**, 2303 (1981).
- ⁴D. J. Chadi, *Phys. Rev. Lett.* **43**, 43 (1979).
- ⁵K. E. Khor and S. D. Sarma, *Phys. Rev. B* **36**, 7733 (1987).
- ⁶F. Bechstedt and D. Reichardt, *Surf. Sci.* **202**, 83 (1988).
- ⁷B. I. Craig and P. V. Smith, *Surf. Sci. Lett.* **226**, L55 (1990).
- ⁸N. Roberts and R. J. Needs, *Surf. Sci.* **236**, 122 (1990).
- ⁹A. Mazur and J. Pollmann, *Surf. Sci.* **225**, 72 (1990).
- ¹⁰J. E. Northrup, *Phys. Rev. B* **44**, 1419 (1991).
- ¹¹F. F. Abraham and I. P. Batra, *Surf. Sci.* **163**, L752 (1985).
- ¹²W. S. Yang, F. Jona, and P. M. Marcus, *Phys. Rev. B* **28**, 2049 (1983).
- ¹³F. J. Himpsel and Th. Fauster, *J. Vac. Sci. Technol. A* **2**, 815 (1983).
- ¹⁴Y. J. Chabal, *Surf. Sci.* **168**, 594 (1986).
- ¹⁵S. Ciraci, R. Butz, E. M. Oellig, and H. Wagner, *Phys. Rev. B* **30**, 711 (1984).
- ¹⁶S. Maruno, H. Iwasaki, K. Horioka, S. T. Li, and S. Nakamura, *Phys. Rev. B* **27**, 4110 (1983).
- ¹⁷C. C. Cheng and J. T. Yates, *Phys. Rev. B* **43**, 4041 (1991).
- ¹⁸K. Oura, J. Yamane, K. Umezawa, M. Naitoh, F. Shoji, and T. Hanawa, *Phys. Rev. B* **41**, 1200 (1990).
- ¹⁹F. Stucki, J. A. Schaefer, J. R. Anderson, G. J. Lapeyre, and W. Göpel, *Solid State Commun.* **47**, 795 (1983).
- ²⁰K. C. Pandey, in *Proceedings of the 17th International Conference on the Physics of Semiconductors, San Francisco, 1984*, edited by D. J. Chadi and W. A. Harrison (Springer-Verlag, New York, 1985), p. 55.
- ²¹L. C. Feldman, P. J. Silverman, and I. Stensgaard, *Nucl. Instrum. Meth.* **168**, 589 (1980).
- ²²R. M. Tromp, R. G. Smeenk, and F. W. Saris, *Phys. Rev. Lett.* **46**, 939 (1981).
- ²³R. M. Tromp, R. G. Smeenk, F. W. Saris, and D. J. Chadi, *Surf. Sci.* **133**, 137 (1983).
- ²⁴Y. J. Chabal and K. Raghavachari, *Phys. Rev. Lett.* **54**, 1055 (1985).
- ²⁵B. W. Holland, C. B. Duke, and A. Paton, *Surf. Sci.* **140**, 1269 (1984).
- ²⁶Y. S. Shu, W. S. Yang, F. Jona, and P. M. Marcus, in *The Structure of Surfaces*, edited by M. A. van Hove and S. Y. Tong (Springer, New York, 1985), p. 293.
- ²⁷J. Boland, *Phys. Rev. Lett.* **65**, 3325 (1990).
- ²⁸R. J. Hamers, R. M. Tromp, and J. E. Demuth, *Phys. Rev. B* **34**, 5343 (1986).
- ²⁹R. Wiesendanger, D. Bürgler, G. Tarrach, and H.-J. Güntherodt, *Surf. Sci.* **232**, 1 (1990).
- ³⁰J. Boland, *Surf. Sci.* **261**, 17 (1992).
- ³¹C. Weakliem, G. W. Smith, and E. A. Carter, *Surf. Sci.* **232**, L219 (1990).
- ³²M. Aono, Y. Hou, C. Oshima, and Y. Ishizawa, *Phys. Rev. Lett.* **49**, 567 (1982).
- ³³J. E. Griffith and G. P. Kochanski, *CRC Crit. Rev. Solid State Mater. Sci.* **16**, 255 (1990); D. Haneman, *Rep. Prog. Phys.* **50**, 1045 (1987); M. A. Schluter, in *The Chemical Physics of Solid Surface Heterogeneous Catalyst*, edited by D. A. King and D. P. Woodruff (Elsevier, Amsterdam, 1988), Vol. 5, p. 37; R. I. G. Uhrberg and G. V. Hansson, *CRC Crit. Rev. Solid State Mater. Sci.* **17**, 133 (1991); J. A. Schaefer, *Physica B* **170**, 45 (1991).
- ³⁴M. Shi, Y. Wang, and J. W. Rabalais, following paper, *Phys. Rev. B* **48**, 1689 (1993).
- ³⁵R. A. Wolkow, *Phys. Rev. Lett.* **68**, 2636 (1992).
- ³⁶K. Kato, T. Ide, T. Nishimori, and T. Ichinokawa, *Surf. Sci.* **207**, 177 (1988).
- ³⁷H. Wang, R. Lin, and X. Wang, *Phys. Rev. B* **36**, 7712 (1987).
- ³⁸J. W. Rabalais, *CRC Crit. Rev. Solid State Mater. Sci.* **14**, 318 (1988).
- ³⁹O. Grizzi, M. Shi, H. Bu, and J. W. Rabalais, *Rev. Sci. Instrum.* **61**, 740 (1990).
- ⁴⁰C. C. Hsu and J. W. Rabalais, *Surf. Sci.* **256**, 77 (1991).
- ⁴¹A. Ishizaka and Y. Shiraki, *J. Electrochem. Soc.* **133**, 666 (1986).
- ⁴²J. W. Rabalais, *Science* **250**, 521 (1990).
- ⁴³F. Masson and J. W. Rabalais, *Chem. Phys. Lett.* **179**, 63 (1991); F. Masson, H. Bu, M. Shi, and J. W. Rabalais, *Surf. Sci.* **249**, 313 (1991).
- ⁴⁴J. W. Rabalais, *J. Vac. Sci. Technol. A* **9**, 1293 (1991).
- ⁴⁵E. S. Mashkova and V. A. Molchanov, *Medium-Energy Ion Reflection From Solids* (North-Holland, Amsterdam, 1985).
- ⁴⁶H. Bu, M. Shi, and J. W. Rabalais, *Nucl. Instrum. Meth. Phys. Res.* **61**, 337 (1991).
- ⁴⁷Y. Lifshitz, S. R. Kasi, J. W. Rabalais, and W. Eckstein, *Phys. Rev. B* **41**, 10468 (1990).

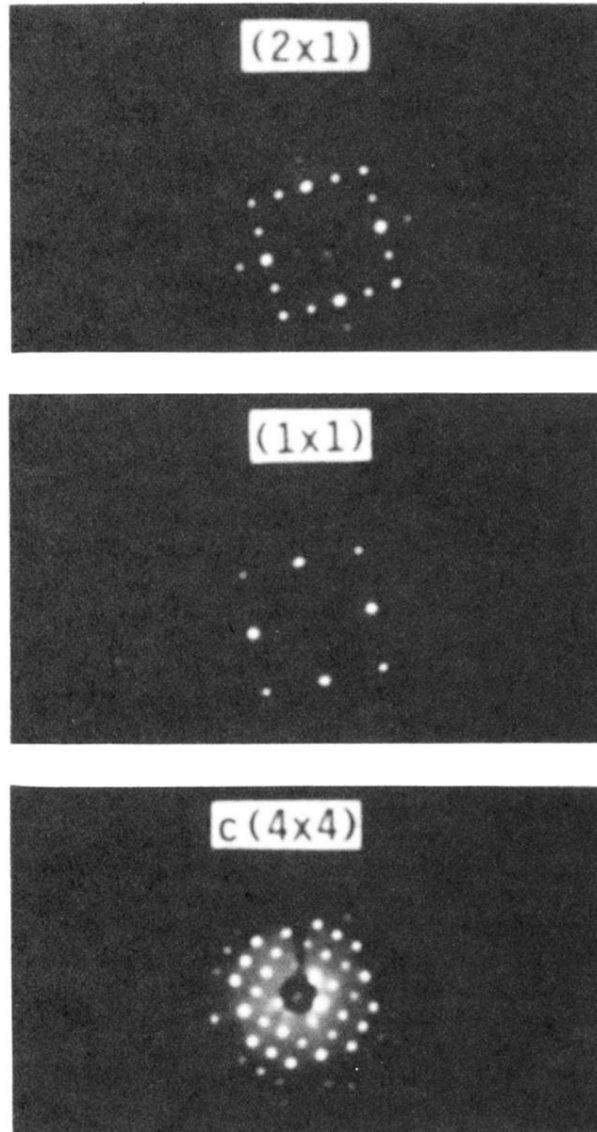


FIG. 1. Observed LEED patterns for the (2×1) -H, (1×1) -H, and $c(4\times 4)$ -H phases of $\text{Si}\{100\}$. The (2×1) pattern represents a superposition of two structural domains, i.e., (2×1) and (1×2) , rotated by 90° . The LEED pattern of the clean (2×1) surface is similar to that shown here for the (2×1) -H surface. Electron energy is 50 eV.